Definition and Application of Variable Resistance Coefficient for Wheeled Mobile Robots on Deformable Terrain

Liang Ding, *Senior Member, IEEE*, Lan Huang, Shu Li, Haibo Gao, Huichao Deng, Yuankai Li, *Senior Member, IEEE*, and Guangjun Liu, *Senior Member, IEEE*

***Abstract*—Resistance coefficient (*RC*) is an important measure when designing wheel-driving mechanisms and accurate dynamic models for real-time mobility control of wheeled mobile robots (WMRs). This measure is typically formulated as a constant that depends on the wheel load, wheel dimensions, and soil that the WMR is designed for. This article proposes a novel variable *RC* that responds to terrain deformation. This variable *RC* is then applied to controllers for WMRs that estimate driving torques and slip ratios on deformable terrain. Simple yet accurate models of *RC* are developed from both experimental results and theoretical analysis, and these models are then compared with other methods. The proposed *RC* models give more accurate and more computationally efficient estimations of driving torques and slip ratios for WMRs, with average estimation errors less than 6% and the shortest computation time in experiments. The two proposed estimators are then applied to the design of the tracking-control systems for a WMR running on deformable terrain. Experiments with simulated sandy terrain demonstrate that both proposed control systems are feasible, and the slip estimation effectively decreases velocity tracking errors from more than 20% to less than 10%.**

***Index Terms*—Deformable terrain, planetary exploration rovers, resistance moment, slip, terramechanics, wheeled mobile robots (WMRs).**

NOMENCLATURE I

Group	Symbol	Parameter and unit
Wheel parameters	J	wheel inertia (kg·m^3)
	m_w	wheel's mass (kg)
	r, r_s	radius and shearing radius of a wheel (m)
	h	height of wheel lug (m)
Motion state variables	x, z	displacement and sinkage (m)
	l, e	normal and tangential distances from wheel center to equivalent contact point (m)
	v	linear velocity of a wheel (m/s)
	ω	angular velocity of a wheel (rad/s)
	ϕ	rotation angle of a wheel (rad)
Interaction mechanics and coefficients	F_{DP}, F_{RC}, F_N, F_T	drawbar pull, compaction resistance, normal force, and tractive force (N)
	W, f	wheel's load in the normal direction and tangential force exerted on the wheel by the robot's body (N)
	M_{DR}, T_D, T_{De}	resistance moment acing on a wheel, desired driving torque and the resistance moment due to terrain deformation (Nm)
	RC, PC, TC	resistance, pull and traction coefficients

NOMENCLATURE II

Group	Symbol	Parameter and unit
Wheel parameters	b	wheel width (m)
Terrain parameters	c	cohesion of soil (kPa)
	k_c	cohesive modulus of soil (kPa/m^{n-1})
	k_φ	frictional modulus of soil (kPa/m^n)
	n	sinkage exponent of soil
	ρ	bulk density of soil (kg/m^3)
	φ	internal friction angle of soil (°)
	K	shearing deformation modulus of terrain
Motion state variables	t	time (s)
	s	slip ratio
Interaction mechanics and coefficients	$\bar{F}_{DP}$, $\bar{F}_N$, $\bar{T}_D$	the average F_{DP}, F_N (N) and T_D (Nm)
	$\overline{TC}$, $\overline{RC}$, $\overline{PC}$	the average RC, PC and TC

Manuscript received July 24, 2019; accepted February 28, 2020. This work was supported in part by the National Natural Science Foundation of China under Grant 51822502 and Grant 91948202, in part by the National Key Research and Development Program of China under Grant 2019YFB1309500, in part by the Fundamental Research Funds for the Central Universities under Grant HIT.BRETIV.201903, and in part by the "111 Project" under Grant B07018. This article was recommended for publication by Associate Editor R. Vasudevan and Editor M. Yim upon evaluation of the reviewers' comments. *(Corresponding authors: Liang Ding; Huichao Deng.)*

Liang Ding, Lan Huang, Shu Li, and Haibo Gao are with the State Key Laboratory of Robotics and Systems, Harbin Institute of Technology, Harbin 150080, China (e-mail: liangding@hit.edu.cn; huanglanxyz@163.com; li_shu43@hotmail.com; gaohaibo@hit.edu.cn).

Huichao Deng is with the Beihang University, Beijing 100191, China (e-mail: denghuichao@buaa.edu.cn).

Yuankai Li and Guangjun Liu are with the Department of Aerospace Engineering, Ryerson University, Toronto, ON M5B 2K3, Canada (e-mail: yuankai.li@uestc.edu.cn; gjliu@ryerson.ca).

Color versions of one or more of the figures in this article are available online at https://ieeexplore.ieee.org.

Digital Object Identifier 10.1109/TRO.2020.2981822

NOMENCLATURE III

Group	Symbol	Parameter and unit
Terrain parameters	c_1, c_2, c_3	coefficients of wheel–soil interaction angle
	N	the linear sinkage exponent of soil that can reflect the slip sinkage phenomena
	n_0, n_1	coefficients for calculating the sinkage exponent N
	K_s	equivalent sinkage modulus of wheel–terrain interaction (kPa/m^n)
Motion state variables	j	terrain deformation (m)
	$\tilde{z}$	equivalent wheel sinkage (m)
	ϕ ,θ_1, θ_2, θ_m	a wheel's rotation, entrance, leaving and maximum stress angle of a wheel (°)
Interaction stress	σ, σ_1, σ_2	normal stress, and the one from angle θ_m to θ_1 , from angle θ_2 to θ_m (kPa)
	τ, τ_1, τ_2	shearing stress and the one from angle θ_m to θ_1, from angle θ_2 to θ_m (kPa)
Parameters of RC models	k_{RC}^{s} , $k_{\mathrm{RC}}^{\theta_1}$	slopes of linearized models of RC versus s and θ_1
	RC_0^s , $RC_0^{\theta_1}$	intercepts of linearized models of RC versus s and θ_1

NOMENCLATURE IV

Group	Symbol	Parameter and unit
Matrices	$\boldsymbol{M}$, $\boldsymbol{A}$, $\boldsymbol{G}$, $\boldsymbol{B}$	matrices of mass, centripetal force, gravity, input transformation
	$\boldsymbol{K}_P$, $\boldsymbol{K}_I$, $\boldsymbol{K}_D$	gain matrices of PID controller
Vectors	$\boldsymbol{F}_R$	resistance of follower wheel (N, Nm)
	$\boldsymbol{F}_{DP}=\left[F_{DP}^{l},F_{DP}^{r}\right]^{T}$	drawbar pulls of left and right wheels (N)
	$\boldsymbol{F}_{N}=\left[F_{N}^{l},F_{N}^{r}\right]^{T}$	normal forces of left and right wheels (N)
	$\boldsymbol{\tau}=\left[\tau_l \quad \tau_r\right]^{T}$	torque inputs of left and right wheels
	$\boldsymbol{T}_D$, $\boldsymbol{T}_{De}$	desired driving torques and resistance torques due to terrain deformation (Nm)
	$\boldsymbol{k}_{RC}^{s}$, $\boldsymbol{RC}_0^{s}$	k_{RC}^{s} s and RC_0^{s} s of driving wheels
	$\boldsymbol{q}=\left[x \;\; y \;\; z \;\; \psi \;\; \theta \;\; \phi\right]^{T}$	the 6-DOF pose of the WMR (m, rad)
	$\boldsymbol{v}=\left[v \quad \omega\right]^{T}$	the body velocity (m/s, rad/s)
	$\boldsymbol{v}_d$, $\boldsymbol{v}_c$, $\boldsymbol{v}_e$	desired and current body velocities and the velocity error (m/s, rad/s)
	$\boldsymbol{\vartheta}=\left[\vartheta_l,\vartheta_r\right]^{T}$	rotation angles of left and right wheels (rad)
	$\boldsymbol{s}=\left[s_l,s_r\right]^{T}$	slip ratios of left and right wheels
	$\boldsymbol{RC}$	RC of driving wheels
	$\hat{\boldsymbol{T}}_{De}$	the estimated $\boldsymbol{T}_{De}$ (Nm)
	$\boldsymbol{F}_{DP}^{d}$	desired drawbar pulls (N)
	$\boldsymbol{\tau}_e$	the torque outputs from PID controller
Parameters of the WMR	d_1, d_2	normal and tangential distances between centroid and driving wheel center (m)
	d_3, d_4	distances between steering shaft of follower wheel and centroid, follower wheel center (m)
Motion state variables	ϑ_{rear}	steering angle of follower wheel (rad)
	F_{rear}^{y} , F_{rear}^{x}	the axial and tangential resistances of the follower wheel (N)
Coordinate system	$\Sigma_I\left(X_I,Y_I,Z_I\right)$	world coordinate system (m)
	$\Sigma_m\left(x_m,y_m,z_m\right)$	body coordinate system (m)

NOMENCLATURE V

Group	Symbol	Parameter and unit
Vectors	$\hat{s}$	the estimated slip ratio
	$\boldsymbol{RC}_{Est}$	the estimated RC
	$\hat{\boldsymbol{v}}_c$	the estimated current body velocity
	ϑ_d , ϑ_c , ϑ_e	desired, current rotation angle of driving wheel and the error (rad)
	$\bar{\boldsymbol{T}}_{De}$	average resistance torque due to terrain deformation (Nm)
	$\boldsymbol{\tau}_e^{\vartheta}$, $\boldsymbol{\tau}_s$, $\boldsymbol{\tau}_c$	the PID regulated torque of angular speed, the slip compensation torque and the measured driving torque (Nm)
Matrix	$\boldsymbol{J}$	Jacobian matrix

I. INTRODUCTION

WHEELED mobile robots (WMRs), such as rovers designed for exploration of the Moon and Mars, need to traverse natural environments that are characterized by rough terrain covered with loose soil [1]–[4]. As the locomotion mechanism moves on such deformable terrain, the WMR wheels might slip significantly [5]. The resulting decrease in velocity can negatively impact the accuracy of location tracking [2], path following [6], and trajectory tracking [7]. Meanwhile, the driving wheels might also suffer from large moments of variable resistance due to terrain deformation [8], which will create large errors in calculations of the desired driving torque (T_D) in simulations [9]–[12], locomotion system design [13]–[15], and dynamic motion control [16].

Considering that certain amount of slip is needed to increase the traction of the WMR on such terrain, the general solution of these problems is compensating for the losses of velocity and driving torque with the estimations of the actual wheel slip and the desired driving torque [17].

Terramechanics-based models are highly accurate and widely used [18]–[23], but the equations are too complex to use for practical estimation of the desired driving torque T_D [24]. Inspired by White *et al.* [25] and Li *et al.* [26], who consider the T_D of a wheel on nondeformable terrain as the production of the wheel radius r and drawbar pull F_{DP}, we determine T_D of a wheel on deformable terrain as $T_D = (F_{\mathrm{DP}} + F_{\mathrm{RC}})r$, where the compaction resistance F_{RC} resulting from terrain deformation can also be regarded as a rolling resistance [8], [27]. The well-known Bekker's equation regards F_{RC} as a function of wheel sinkage [21], [28], but this model is very inaccurate for wheels with diameters smaller than 500 mm, particularly in scenarios involving high slip sinkage [28]. An experimental study found that F_{RC}, which takes up a part of T_D, increases along with the slip ratio [29]. Based on experimental observations, a semi-empirical terramechanics model that simplifies the Wong–Reece model [30] by linearly approximating shear and normal stress equations has been deduced [31], [32], decoupled [33], and extended to dynamic processes [34], [35]. However, such models are still complicated as they include all terrain parameters. Recently in [36], a dynamic model formulation that employs numerical force-balance optimization and meets

Manuscript 3128 submitted to 2020 IEEE/RSJ International Conference on Intelligent Robots and Systems. Received May 21, 2020.

requirements of both high fidelity and computational efficiency for real-time motion control of WMRs is reported, and the model is compared with the terramechanics model which realizes real-time computation by precomputing a lookup table. However, both the parameter identification of multibody system and the construction of a full lookup table for multi terrains are difficult to realize in practice.

Like driving torque, slip also plays an important role in terramechanics and it has received considerable research attention. Wheel slip can be detected by comparing the linear velocity of the center of the wheel with the calculated angular velocity of the wheel. The former is estimated by integrating a linear acceleration measurement and the latter is obtained by using encoder measurements [37], [38]. To improve accuracy, GPS data is also commonly introduced into the system [39]. In planetary environments where GPS data is not available, accurate linear velocity measurements can be recorded with visual odometry modules [40], [41]. Cooperative localization with multiple robots can potentially deliver the velocity of each robot [42], [43]. Another approach for estimating slip is the visual observation of wheel traces on soft terrain, and the calculation cost for this method is lower than that of visual odometry [44]. However, the severe time delay involved in these methods limits their application to motion control systems of WMRs.

Kinematic motion control methods with slip estimation for WMRs on deformable terrain have been reported [45]. In reality, however, such wheeled mobile systems are significantly affected by wheel-slip dynamics [16]. Adaptive control strategies are used for dynamic control of WMRs on deformable terrain, and they consider the effects of terrain deformation as unknown parameters [46] or nonparameter uncertainties [47], [48]. Other methods use neural networks [49] and fuzzy control logic [50]. Compared with previous approaches, these new strategies are more effective and efficient for dealing with terrain uncertainties, but their implementations are complex and associated with very high calculation cost, limiting their practical use.

This article focuses on providing an intrinsic model of variable resistance coefficient (RC), including experimental study, theoretical modeling, parameter identification, and the examples of applications. The main contributions of this article lie in the following: 1) from the perspective of terramechanics, provide an intrinsic model of *RC* with characteristics of high efficiency, easy understanding and high accuracy, based on experimental investigation and theoretical derivation; 2) from the perspective of control, provide a more feasible and efficient method for estimation of the desired driving torque and slip ratio with variable *RC* to improve the tracking control performance, demonstrating the parameter identification and application approach of the *RC* model.

The rest of this article is organized as follows. Section II defines the variable *RC* measure and presents an experimental study of *RC*. Section III analyzes how the value of the *RC* is affected by several relevant factors. Section IV derives models for calculating *RC*. Section V describes a tracking control system for a WMR with the driving torque estimated from *RC*. Similarly, Section VI proposes a velocity-compensation controller for a WMR that estimates the slip ratio from *RC*. Section VII concludes this article.

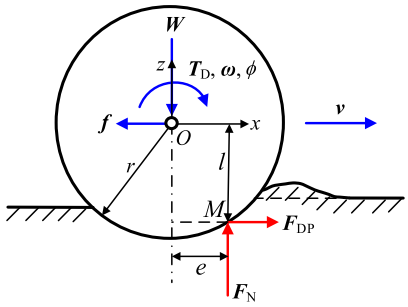

Fig. 1. Forces and torque acting on a driving wheel (parameters and variables in the figure are listed in Nomenclature).

II. Variable Coefficients for Calculating Wheel–Soil Interactions

In this section, we analyze the interactions of a wheel rolling on deformable terrains, and accordingly, define the variable *RC* of the wheel. Similarly, the variables pull and traction coefficients (*PC* and *TC*, respectively) are also defined based on the results of force analysis.

Assume that the terrain is homogenously filled with soft sand and the terrain surface adjacent to a wheel is even. Fig. 1 shows the forces and torque that act on a driving wheel due to the soil, vehicle body, and driving motor. In Fig. 1, $e^2 + l^2 = r^2$. The normal force F_N and drawbar pull F_{DP} that balance a wheel can be estimated through quasi-static analysis or measured using a force/torque (F/T) sensor.

This section deduces equations for estimating the torque required to drive a wheel according to F_N and F_{DP}.

For such wheel moving with some acceleration, the following equilibrium equations can be obtained with the mass of the wheel m_w:

$$F_N - W - m_w\ddot{z} = 0 \tag{1a}$$

$$F_{\mathrm{DP}} - f - m_w\ddot{x} = 0 \tag{1b}$$

$$T_D - M_{\mathrm{DR}} - J\ddot{\phi} = 0 \tag{1c}$$

$$M_{\mathrm{DR}} = F_{\mathrm{DP}} \cdot l + F_N \cdot e. \tag{1d}$$

If the robot moves with a constant velocity or in a quasi-static state with low acceleration, one can estimate the desired driving torque for a wheel based on (1)

$$T_D = M_{\mathrm{DR}} = F_{\mathrm{DP}} \cdot l + F_N \cdot e. \tag{2}$$

Considering that *l* is very close to *r*, a simplified form of the above equation is obtained as follows:

$$T_D \approx F_{\mathrm{DP}} r + F_N e. \tag{3}$$

Generally, the simplification error of T_D is lower than 5% [27], [51]. By combining (3) with conventional rolling mechanics model $F_T = T_D/r = F_{\mathrm{DP}} + F_{\mathrm{RC}}$, the effective drawbar pull is derived

$$F_{\mathrm{DP}} \approx T_D/r - F_N \cdot (e/r) = F_T - F_{\mathrm{RC}} \tag{4}$$

where F_{RC} indicates the compaction resistance and F_T is the tractive force.

Manuscript 3128 submitted to 2020 IEEE/RSJ International Conference on Intelligent Robots and Systems. Received May 21, 2020.

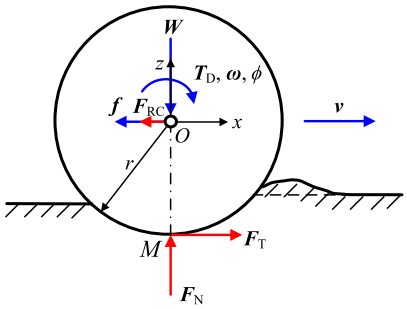

Fig. 2. Equivalent forces acting on a wheel corresponding to (4).

Fig. 3. Wheel–soil interaction testbed and experimental wheel.

Fig. 2 shows the equivalent contact forces acting on a wheel corresponding to (4).

Define $RC = F_{\mathrm{RC}}/F_N$ as the resistance coefficient, and let $T_{De} = F_{\mathrm{RC}}r$ represent the extra rolling resistance torque acting on the wheel, which is resulted from terrain deformation. The desired driving torque can be calculated with *RC* or T_{De} as follows:

$$T_D = F_T r \approx F_{\mathrm{DP}} r + F_{\mathrm{RC}} r = F_{\mathrm{DP}} r + F_N r \cdot RC = F_{\mathrm{DP}} r + T_{De}. \quad (5)$$

It should be noted that *RC* is a ratio of compaction resistance to normal force on one hand, reflecting the driving resistance under a certain load, as shown in Fig. 2. On the other hand, *RC* can also be used for calculating T_{De}, reflecting the rolling resistance torque under a certain load, as shown in Fig. 1 ($T_{De} = F_N r \cdot RC = F_N \cdot e$).

The other issue is determining the value of *RC*, which is usually considered as a constant for a certain pair of contact objects. However, for a rigid wheel moving on a deformable rough terrain, *RC* varies as the function of the motion state variables. Given F_N, F_{DP}, and *RC*, the desired driving torque can be estimated using (5). Given T_D, F_N, and *RC*, the drawbar pull acting on a wheel by the terrain can be estimated using (4).

The pull coefficient (*PC*) is defined as the ratio of drawbar pull to normal force, while the traction coefficient (*TC*) is defined as the ratio of tractive force to normal force [27]. They reflect the pull and tractive ability of a wheel under a certain load, respectively. The values of *TC* and *PC* are

$$TC = T_D/(F_N r). \quad (6a)$$

$$PC = F_{\mathrm{DP}}/F_N. \quad (6b)$$

For a wheel with lugs of height *h*, the value of *TC* becomes

$$TC = T_D/(F_N r_{\mathrm{s}}) \quad (7)$$

where r_{s} is the shearing radius and $r_s = r + \lambda_s h (0 \le \lambda_s \le 1)$ [22]. The value of λ_s is 0.65 and 0.75 for lug heights of 10 and 15 mm, respectively.

Based on (5) and (6), the value of *RC* is estimated as follows:

$$RC \approx T_D/(F_N r) - F_{\mathrm{DP}}/F_N = TC - PC. \quad (8)$$

According to (8), for redundant driving multiwheeled mobile robots traversing on uneven deformable terrains, the objective is to minimize the values of *TC*s by reducing the demand of *PC*s for driving wheels and minimizing the values of *RC*s by using coordinated control for reducing wheel slips.

III. Study of *RC* Variation With Relevant Factors

In this section, the variation of *RC* is experimentally studied through a wheel–soil interaction testbed and a series of rigid test wheels. The effects of various factors (time, slip ratio, sinkage, entrance angle and wheel properties) on *RC* are discussed based on the experimental results.

A. Experimental Study

In order to figure out the variation of *RC* with motion state variables and wheel parameters, a wheel–soil interaction testbed (see Fig. 3) was used for measuring the wheel sinkage, normal force, drawbar pull, and driving torque [27].

The testbed has dimensions of 1700 × 850 × 900 mm, equipped with two motors (driving motor and carriage motor) and corresponding sensors (a displacement sensor, a six-axis F/T sensor, a driving torque sensor and two encoders). The driving motor drives the tested wheel, while the carriage motor creates a certain slip ratio, simulating the effects of rover body on an installed wheel. The wheel sinkage, z, was obtained by measuring the normal displacement of the wheel's bottom relative to the surface of sand in the soil bin with a high-precision linear-potentiometer displacement sensor. The sensor was calibrated before carrying out experiments. The rotating wheel was lowered so that the lugs make contact with the soil by adjusting the height of the sustaining jack. The value of z was set to $-h$ when the lowest point of wheel lugs reached the sand, ensuring zero value of z when the wheel bottom touched the sand. At that point, we put the wheel down on the sand surface and controlled the wheel to move forward; the value of z then increased and was measured in real-time while the wheel moving forward and sinking. The F/T sensor is used for measuring the drawbar pull, normal force of the wheel, while the driving torque of the motor is measured by the torque sensor.

Three types of cylindrical metal wheels with different dimensions were used. The wheel dimensions used herein are comparable to those used in most recent planetary rovers, as shown in Table I. For easy reading, the wheels are named depending on their sizes. Accordingly, the capital letter represents that the wheel is larger size than wheels named in lowercase.

Manuscript 3128 submitted to 2020 IEEE/RSJ International Conference on Intelligent Robots and Systems. Received May 21, 2020.

TABLE I
SIZES OF THE WHEELS

Wheel	Wh-RBH	Wh-RBh	Wh-rbH	Wh-rbh	Wh-rBH	Wh-rBh
r (mm)	157.35	157.35	135	135	135	135
b (mm)	165	165	110	110	165	165
h (mm)	15	10	15	10	15	10

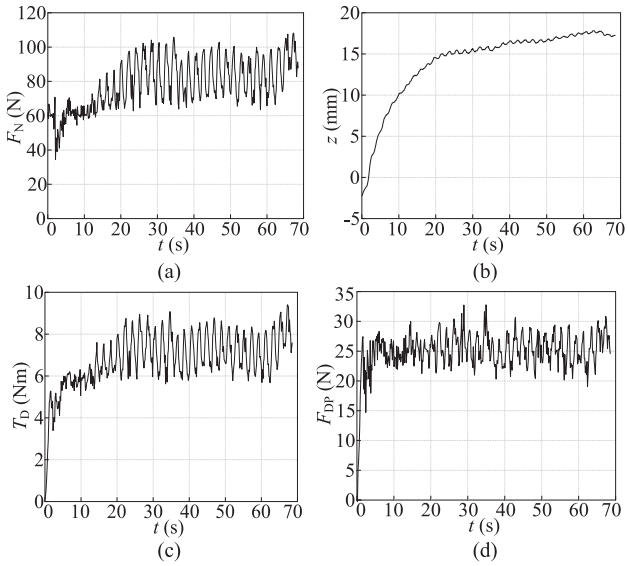

Fig. 4. Raw force/sinkage measurements (Wh-RHB, $s = 0.4$, $W = 80$ N).

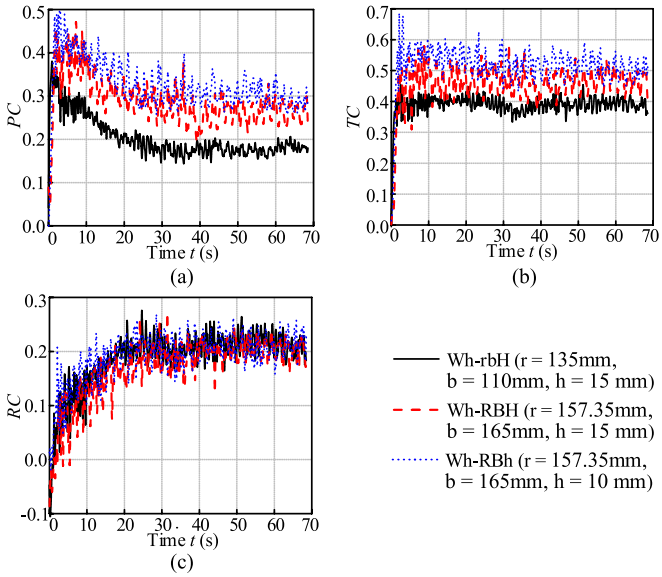

Fig. 5. Variation of *PC*, *TC*, and *RC* with time for rigid wheels of different sizes ($s = 0.4$, $W = 80$ N).

The terrain was made of soft sand, the mechanical property parameters of which are as follows [33]: $k_c = 15.6$ kPa/m^{n-1}, $k_\varphi = 2407.4$ kPa/m^n, $c = 0.25$ kPa, $\varphi = 31.9°$, $K = 9.7$–13.1 mm, and $\rho = 1605$ kg/m^3. The soil was made uniform and smooth with the ripper and strickling mechanism. This is very important to ensure the repeatability of the experimental results as shown in Fig. 4.

The motion state variables were set according to those of the current planetary exploration rovers. A wheel should be controlled to move with slip ratio smaller than 0.6, as the wheel moves with very high slip-sinkage when the slip ratio is larger than 0.6 [27]. Thus, the experimental slip ratios were set as 0–0.6, and the linear velocity was set to 10 mm/s. The vertical load in most of the experiments was 80 N, which was set with consideration of the load capacity of the testbed and fluctuation amplitude of the measured wheel load. In addition, vertical loads of 30 and 150 N were also exerted on Wh-RBh for investigating the load effect (as reported in [55], the wheel loads of China's Yutu lunar rover on the moon are close to 30 N).

In the experiments, the wheel sinkage gradually increases to a relatively steady value, and the original experimental results fluctuate as the wheel lugs enter into and leave the soil, as shown in Fig. 4. Driving torque and drawbar pull increase considerably faster than wheel sinkage. The steady-state experimental results are used for calculating the average values.

B. RC Variation as a Function of Time

The variation of *RC* with time is studied with experiments. Equations (6) and (8) are combined for calculating *RC* as a function of time t

$$RC(t) \approx TC(t) - PC(t) = T_D(t)/[F_N(t) r_s] - F_{\mathrm{DP}}(t)/F_N(t). \quad (9)$$

Fig. 5 shows the results of traction coefficient *TC*, pull coefficient *PC*, and resistant coefficient *RC* for wheels Wh-rbH, Wh-RBH, and Wh-RBh.

At the outset, *TC* and *PC* increase rapidly from zero to large values. Then, *TC* fluctuates steadily, but *PC* decreases gradually to a smaller steady-state value. The *TC* is hardly influenced by wheel sinkage, but the *RC* increases with an increase in wheel sinkage, thus leading to a decrease in *PC*. The *TC* and *PC* increase with the height of wheel lugs, but *RC* is more sensitive to wheel sinkage than to the wheel lugs.

C. RC Versus Slip Ratio

The variation of *RC* with slip ratio s in the steady state is studied with experimental results. Under a certain slip ratio s, (10) is used for calculating the average resistance coefficient *RC* in the steady state (for example, the data obtained from 30 to 60 s in Fig. 6)

$$RC \approx TC - PC = \bar{T}_D/(\bar{F}_N r_s) - \bar{F}_{\mathrm{DP}}/\bar{F}_N. \quad (10)$$

The s of a wheel could be divided into three phases: rising phase, transitional phase, and high slip-sinkage phase [27]. If s ranges from 0 to 0.2, the drawbar pull, driving torque, *PC,* and *TC* increase rapidly with s, whereas these values increase slowly if s increases from 0.2 to 0.6. If s is larger than 0.6, the wheel exhibits severe sinkage on the soft terrain.

Manuscript 3128 submitted to 2020 IEEE/RSJ International Conference on Intelligent Robots and Systems. Received May 21, 2020.

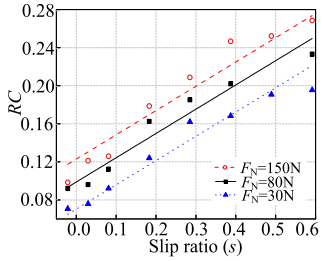

Fig. 6. *RC* versus slip ratio at different loads (Wh-RBh).

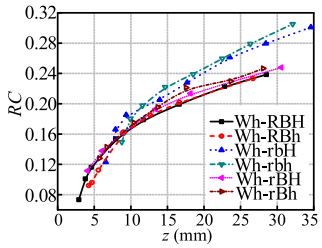

Fig. 7. *RC* versus z for various wheel dimensions.

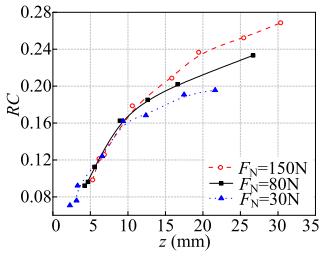

Fig. 8. *RC* versus z for different F_N.

The *RC* is conventionally considered constant and does not change with the slip ratio. However, Fig. 6 illustrates that *RC* is approximately a linear increasing function of s. In Fig. 6, *RC* can be closely approximated by $0.123 + 0.255s$ ($0.099 + 0.255s$, $0.070 + 0.255s$), and the *R*-square value is 94.5% (96.8%, 93.8%), for wheel Wh-RBh with normal load of 150 N (80 N, 30 N).

D. RC Versus Wheel Sinkage

The variation of *RC* with wheel sinkage z in the steady state is studied with experiment. The wheel sinkage z increases rapidly with the increase of slip ratio s. With an increase in z, the values of *TC* and *PC* increase rapidly to a certain value and then increase with a very small slope. The value of *RC* increases with z. According to Fig. 7, the wheel radius and lug height have minor influences on *RC* for the same z, but the wheel with the smaller width has the larger *RC*. And, for the same z, the values of *RC* decrease slightly with a decrease in the normal force F_N.

The curve of *RC* versus z is approximately two-phases piece-wise linear. Although the relationship appears to be nonlinear in the region of 0–15mm sinkage, the linearization error in the full scale is within 6%. In Fig. 8, the cut-off points of two linear functions of *RC* versus z occur at 10–15 mm.

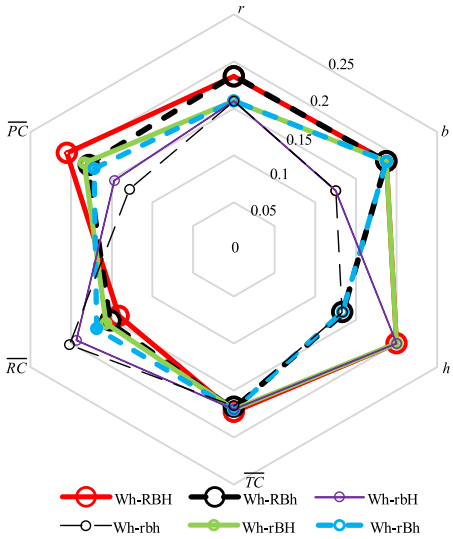

Fig. 9. Normalized values of wheel properties (r, b, h) and normalized average values of *PC*, *TC*, and *RC* under $W = 80$ N.

E. RC Versus Entrance Angle

The variation of *RC* with wheel entrance angle θ_1 in the steady state is studied according to the experimental data plotted in [27], where the values of *RC* did not remain constant with the increase of entrance angle θ_1.

The θ_1 is a nonlinear increasing function of wheel sinkage

$$\theta_1 = a\cos[(r - z)/r]. \tag{11}$$

Thus, for the same entrance angle θ_1, the influences of wheel dimensions and normal force on *RC* are similar to that at the same wheel sinkage z. By observing the data plotted in [27], the positive linear relationship between *RC* and θ_1 is discovered.

F. Influence of Wheel Properties and Load

The variations of *RC* with wheel properties (radius, width, and the height of wheel lugs) and load in the steady state are studied with experimental results. The results of traction coefficient *TC*, pull coefficient *PC*, and resistant coefficient *RC* for different wheels shown in Table I under a vertical load of 80 N are given in [27]. To illustrate how the wheel properties affect these coefficients, a spider diagram is shown in Fig. 9, in which small and large circular marks correspond to wheels with small and large radii, the thin and thick curves correspond to wheels of small and large widths, and the solid and dashed curves correspond to wheels with higher and lower lugs. The average values of coefficients of the tested wheels are listed in Table II.

We find that wheel dimension r has a minor influence on *TC*, but a major influence on *RC* based on Fig. 9. The larger the wheel width or radius, the smaller is *RC*. According to Fig. 9, for wheels Wh-rBH and Wh-RBH, the wheel radius increases

Manuscript 3128 submitted to 2020 IEEE/RSJ International Conference on Intelligent Robots and Systems. Received May 21, 2020.

TABLE II
AVERAGE VALUES OF *TC*, *RC*, AND *PC* FOR DIFFERENT WHEELS

Wheel	Wh-RBH	Wh-RBh	Wh-rbH	Wh-rbh	Wh-rBH	Wh-rBh
$\overline{TC}$	0.382	0.372	0.376	0.367	0.376	0.377
$\overline{RC}$	0.160	0.175	0.219	0.229	0.178	0.191
$\overline{PC}$	0.221	0.197	0.158	0.138	0.198	0.185

TABLE III
AVERAGE VALUES OF *TC*, *RC*, AND *PC* FOR DIFFERENT LOADS

Normal load	30 N	80 N	150 N
$\overline{TC}$	0.392	0.332	0.325
$\overline{RC}$	0.135	0.155	0.186
$\overline{PC}$	0.257	0.177	0.137

TABLE IV
INFLUENCE OF DIFFERENT CONDITIONS ON *TC*, *RC*, AND *PC*

Indices	Wheel lugs	Dimension	Load
TC	Small	Small	Large negative
RC	Large negative	Large negative	Large positive
PC	Large positive	Large positive	Very large negative

16.6%, $\overline{TC}$ increases 1.6%, $\overline{RC}$ decreases 10.1%, and the resultant $\overline{PC}$ increases 11.6%. For wheels Wh-rbH and Wh-rBH, the width increases 50%, values of $\overline{TC}$ are almost the same, $\overline{RC}$ decreases 18.7%, and the resultant $\overline{PC}$ increases 25.3%. For wheels Wh-rBh (Wh-RBh, Wh-rbh) with lugs of 10 mm in height and Wh-rBH (Wh-RBH, Wh-rbH) with lugs of 15 mm in height, $\overline{PC}$ increases 7.0% (12.2%, 14.5%), $\overline{TC}$ increases 2.5% (2.7%, –0.3%), $\overline{RC}$ decreases 6.8% (8.6%, 4.4%). This is because the lugs of 10 mm height almost play an adequate role in shearing. On this basis, the increase of their height will only improve their impact on supporting, similar to slightly increasing *r*, and thereby the *RC* slightly decreases. Considering the results shown in Fig. 9, one can conclude that for normal wheel with lugs in reasonable size, the increment of *PC* is mainly due to the decrease of *RC* for wheels with larger lug height.

The $\overline{TC}$, $\overline{PC}$, and $\overline{RC}$ under different slip ratios reflecting the load effect are listed in Table III. With a decrease in the normal load acting on a wheel, the pull coefficient is increased by both increasing *TC* and decreasing *RC*. When the load increases from 30 to 80 N (166.7%), $\overline{TC}$ decreases 15.3%, $\overline{RC}$ increases 14.8%, and the resultant $\overline{PC}$ decreases 31.1%. When the load increases from 30 to 150 N (400%), $\overline{TC}$ decreases 17.1%, $\overline{RC}$ increases 37.8%, and the resultant $\overline{PC}$ decreases 46.7%.

According to the above experimental results and analysis, the effects of lug height, wheel dimensions (radius and width), and load are summarized in Table IV. The wheel lugs have a small influence on *TC* and a large positive influence on *RC*, which is similar to the influence of wheel dimensions. As a result, the influence of lugs and wheel dimensions on *PC* is large positive. The load has opposing influences on *TC* and *RC*; thus, its positive influence on *PC* is very large owing to the accumulation effect. The value of *PC* increases with the increase of lug height and wheel radius/width, but decreases with the increase of load. To minimize the resistance coefficient and maximize the efficiency of a WMR, one can use the largest wheel dimensions and lug height that are allowable, and reduce the weight of the WMR in order to decrease the vertical loads exerted on the wheels. Furthermore, one should optimally control the tractive forces of different wheels and make them evenly distributed according to the vertical loads to prevent excessive sinkage and slip of the wheels.

IV. RC MODELS

Based on the experimental observation in Section III, empirical *RC* models in a linearized form are introduced in Part A for the *RC* estimation during the phase of operation. Then, alternative terramechanics models of *RC* are derived in Part B based on previous studies [22], [30], allowing *RC* estimation when experimental data collection of force versus slip is not possible.

A. Linearized Model

This section proposes a linearized model for the *RC*, as *RC* almost increases linearly with the increase in the slip ratio *s* or the entrance angle θ_1 according to the above investigation. The intercept and increasing slope are primarily functions of the wheel radius *r*, wheel width *b*, and vertical load *W*. Thus, (12) and (13) are proposed for estimating the resistance coefficient as a linear function of the slip ratio or entrance angle, respectively

$$RC = RC_0^s(r, b, W) + k_{RC}^s(r, b, W)s \tag{12}$$

$$RC = RC_0^{\theta_1}(r, b, W) + k_{RC}^{\theta_1}(r, b, W)\theta_1. \tag{13}$$

As can be seen in Fig. 6, the influence of load on the increasing gradient in the *RC* versus *s* can be neglected. According to the figures of *RC* versus θ_1 in [27], when the entrance angle is smaller than 25°, the influence of load on the intercept of *RC* versus θ_1 is negligible. The dimensions of a given robot's wheels are constant, thus the influence of wheel radius and width on the parameters in (12) and (13) can be ignored for a certain wheel, and the following simplified equations are obtained:

$$RC = RC_0^s(W) + k_{RC}^s s \tag{14}$$

$$RC = RC_0^{\theta_1} + k_{RC}^{\theta_1}(W)\theta_1. \tag{15}$$

If *W* does not change largely, the load effect can be ignored, thus RC_0^s and $k_{\mathrm{RC}}^{\theta_1}$ will have constant values and one obtains:

$$RC = RC_0^s + k_{RC}^s s \tag{16a}$$

$$RC = RC_0^{\theta_1} + k_{RC}^{\theta_1}\theta_1. \tag{16b}$$

B. Relevant Terramechanics Models

The derivations of integral-form terramechanics model and explicit-form analytical model for calculating *RC* are given in this part.

Manuscript 3128 submitted to 2020 IEEE/RSJ International Conference on Intelligent Robots and Systems. Received May 21, 2020.

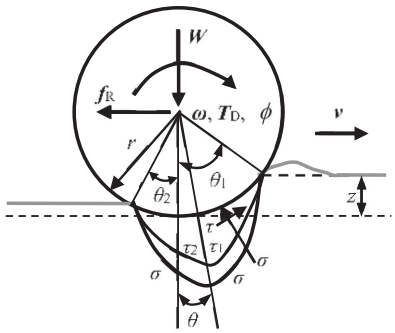

Fig. 10. Stress distributions of wheel–terrain interaction.

1) Integral-Form Terramechanics Model: Fig. 10 shows a diagram of the distributions of normal and shear stress for analyzing wheel–soil interaction mechanics [22], [30]. The wheel interacts with the deformable terrain in the form of a continuous normal stress σ and a shear stress τ, which are divided into a forward part from θ_1 to θ_m (σ_1 and τ_1) and a rear part from θ_m to θ_2 (σ_2 and τ_2). The parameters that influence the interaction stresses include k_c, k_φ, n, c, φ, and K, which could be estimated using the approach proposed in [33].

The entrance angle θ_1 is a function of wheel sinkage z, whereas the leaving angle θ_2 and the maximum-stress angle θ_m are functions of θ_1 and the contact angle parameters of wheel–terrain interaction, i.e., c_1, c_2, and c_3 [22], [30]:

$$\theta_m = (c_1 + c_2 s)\theta_1 \tag{17a}$$

$$\theta_2 = c_3 \theta_1. \tag{17b}$$

The slip ratio s is the most important motion state variable that influences wheel–terrain interaction mechanics, and it is defined as follows:

$$s = \begin{cases} (r\omega - v)/r\omega & (r\omega \geq v, s \in [0,1]) \\ (r\omega - v)/v & (r\omega < v, s \in [-1,0]) \end{cases}. \tag{18}$$

Let $\boldsymbol{F} = [\, F_N \;\; F_{\mathrm{DP}} \;\; T_D \,]^T$ represent the contact mechanics vector. An equation for calculating $\boldsymbol{F}$ by integrating the normal and shear stresses is as follows:

$$\boldsymbol{F} = rb \int_{\theta_2}^{\theta_1} \boldsymbol{R}(\theta)\boldsymbol{S}(\theta) d\theta \tag{19}$$

where

$$\boldsymbol{R}(\theta) = \begin{bmatrix} \cos\theta & \sin\theta \\ -\sin\theta & \cos\theta \\ 0 & r \end{bmatrix} \tag{20a}$$

$$\boldsymbol{S}(\theta) = \begin{bmatrix} \sigma(\theta) & \tau(\theta) \end{bmatrix}^T. \tag{20b}$$

Based on [30], the normal stress $\sigma(\theta)$ and shear stress $\tau(\theta)$ in (20b) can be expressed as follows:

$$\sigma(\theta) = K_s \tilde{z}^N(\theta) \tag{21a}$$

$$\tau(\theta) = [c + \sigma(\theta)\tan\varphi] \times \{1 - \exp(-j(\theta)/K)\}. \tag{21b}$$

Equations for calculating the unknowns in (21) are as follows [22], [30]:

$$K_s = k_c/b + k_\varphi \tag{22a}$$

$$N = n_0 + n_1 s \tag{22b}$$

$$\tilde{z}(\theta) = \begin{cases} r(\cos\theta - \cos\theta_1) & \theta \in [\theta_m, \theta_1] \\ r\{\cos[\theta_1 - (\theta - \theta_2)\frac{\theta_1 - \theta_m}{\theta_m - \theta_2}] - \cos\theta_1\} & \theta \in [\theta_2, \theta_m] \end{cases} \tag{22c}$$

$$j(\theta) = r[(\theta_1 - \theta) - (1 - s)(\sin\theta_1 - \sin\theta)]. \tag{22d}$$

By substituting (21b) into (19), one obtains the driving torque:

$$T_D = r^2 b \int_{\theta_2}^{\theta_1} [c + \sigma(\theta)\tan\varphi] \times \{1 - \exp(-j(\theta)/K)\} d\theta. \tag{23}$$

Upon analyzing equation of drawbar pull in (19), the integration of shear stress yields the tractive force caused by the driving torque, while the integration of normal force is the compaction resistance F_{RC}. The integral-form terramechanics model of resistance coefficient is given as follows:

$$RC = F_{\mathrm{RC}}/F_N = \left[rb \int_{\theta_2}^{\theta_1} \sigma(\theta)\sin\theta d\theta \right] / F_N. \tag{24}$$

2) Explicit-Form Analytical Model: The normal stress and shear stress can be simplified using the linearization method [33], [53]

$$S_i(\theta) \approx \begin{cases} S_{i1}^L(\theta) = S_{im}(\theta_1 - \theta)/(\theta_1 - \theta_m) & \theta \in [\theta_m, \theta_1] \\ S_{i2}^L(\theta) = S_{im}(\theta - \theta_2)/(\theta_m - \theta_2) & \theta \in [\theta_2, \theta_m] \end{cases} \tag{25}$$

where $i = \{1, 2\}$, and $S_1 = \sigma$, $S_2 = \tau$.

By substituting (26) for (19) and integrating the equations, one obtains the analytical equation of interaction mechanics [33], $\tilde{\boldsymbol{F}} = [\, \tilde{F}_{\mathrm{N}} \;\; \tilde{F}_{\mathrm{DP}} \;\; \tilde{T}_{\mathrm{D}} \,]^T$.

According to the study in [53], the explicit-form analytical model of resistance coefficient is as follows:

$$RC = BC/(A^2 + B^2) \tag{26}$$

where

$$A = \frac{\cos\theta_m - \cos\theta_2}{\theta_m - \theta_2} + \frac{\cos\theta_m - \cos\theta_1}{\theta_1 - \theta_m} \tag{27a}$$

$$B = \frac{\sin\theta_m - \sin\theta_2}{\theta_m - \theta_2} + \frac{\sin\theta_m - \sin\theta_1}{\theta_1 - \theta_m} \tag{27b}$$

$$C = (\theta_1 - \theta_2)/2. \tag{27c}$$

V. Tracking Control With Driving Torque Estimation

For planetary exploration, the fast and accurate dynamic tracking control of a planetary rover is necessary. However, the generally unknown resisting moment T_{De} caused by terrain deformation may change significantly with a small increase in the terrain slope, which causes great challenges to the controller. The online estimation of T_{De} and eventually obtaining the desired driving torque T_D by using *RC* is an efficient and effective way to solve this problem, supporting for the dynamic tracking control system designed in this section. Then, the proposed

Manuscript 3128 submitted to 2020 IEEE/RSJ International Conference on Intelligent Robots and Systems. Received May 21, 2020.

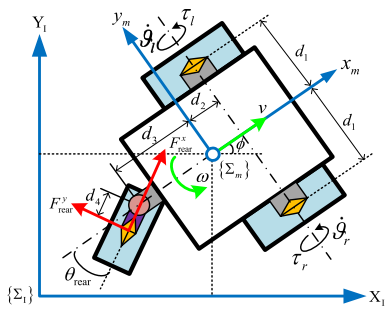

Fig. 11. Model of the (2, 0) type WMR on deformable terrain (the unmentioned variables and parameters in the figure are listed in Nomenclature).

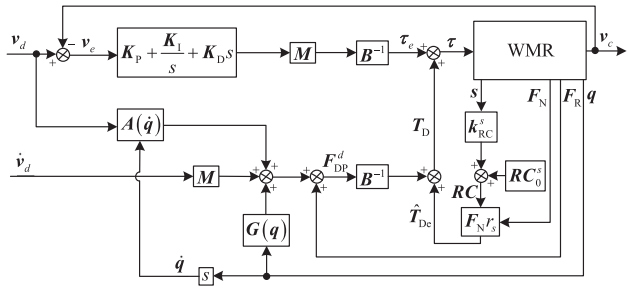

Fig. 12. Velocity tracking control system for the WMR with desired driving torques estimation by using *RC* model ($\boldsymbol{s}$,$\boldsymbol{F}_N$, $\boldsymbol{F}_R$,$\boldsymbol{v}_c$, and $\boldsymbol{q}$ are measured quantities).

RC estimation methods and the tracking control systems are experimentally verified.

A. Tracking Control Algorithm With Torque Estimation

A WMR of (2, 0) type shown in Fig. 11 is described by following dynamic model when it is moving on the deformable terrain:

$$\boldsymbol{M}(\boldsymbol{q})\dot{\boldsymbol{v}}_c + \boldsymbol{A}(\boldsymbol{q},\dot{\boldsymbol{q}})\boldsymbol{v}_c + \boldsymbol{G}(\boldsymbol{q}) = \boldsymbol{B}(\boldsymbol{\tau} - \boldsymbol{T}_{De}) - \boldsymbol{F}_R \tag{28}$$

where $\boldsymbol{q} = [x\ y\ z\ \psi\ \theta\ \phi]^T$ denotes the pose of the WMR, $\boldsymbol{v}_c = [v\ \omega]^T$indicates the body velocity, $\boldsymbol{\tau} = [\tau_l\ \tau_r]^T$are the torque inputs; the $\boldsymbol{M}(\boldsymbol{q})$, $\boldsymbol{A}(\dot{\boldsymbol{q}})$, $\boldsymbol{G}(\boldsymbol{q})$, $\boldsymbol{B}(\boldsymbol{q})$ as well as $\boldsymbol{F}_R$ are respectively the matrices of mass, centripetal force, gravity, input transformation, and resistances of the follower rear wheel detected by an F/T sensor. The actual expressions of these matrices are as follows:

$$\boldsymbol{M} = \begin{bmatrix} m & 0 \\ 0 & I \end{bmatrix} \boldsymbol{A}(\dot{\boldsymbol{q}}) = \begin{bmatrix} 0 & md_2\dot{\phi} \\ 0 & 0 \end{bmatrix}$$

$$\boldsymbol{G}(\boldsymbol{q}) = \begin{bmatrix} mg\sin\theta\cos\psi \\ mgd_2\sin\theta\sin\psi \end{bmatrix} \boldsymbol{B} = \frac{1}{r_s}\begin{bmatrix} 1 & 1 \\ -d_1 & d_1 \end{bmatrix}$$

$$\boldsymbol{F}_R = \begin{bmatrix} -F^x_{\text{rear}}\cos\theta_{\text{rear}} + F^y_{\text{rear}}\sin\theta_{\text{rear}} \\ \left(F^x_{\text{rear}}\sin\theta_{\text{rear}} + F^y_{\text{rear}}\cos\theta_{\text{rear}}\right)(d_4\cos\theta_{\text{rear}} + d_3) \end{bmatrix}.$$

And $\boldsymbol{T}_{De}$ is the matrix of extra driving torques caused by terrain deformation which are usually regarded as unknown disturbances. Now $\boldsymbol{T}_{De}$ can be estimated simply yet accurately through the proposed *RC* linearized model (16a) and (5) as follows:

$$\hat{\boldsymbol{T}}_{De} = r_s \begin{bmatrix} F^l_N\left(RC^s_0 + k^s_{RC}s_l\right) \\ F^r_N\left(RC^s_0 + k^s_{RC}s_r\right) \end{bmatrix} \tag{29}$$

where F^l_N, F^r_N and s_l, s_r are the normal forces and slip ratios of the left and right driving wheels, respectively.

According to model (28), the desired driving torques $\boldsymbol{T}_D$ and drawbar pulls $\boldsymbol{F}^d_{\text{DP}}$ of the two wheels that keep the WMR moving at the desired velocity $\boldsymbol{v}_d = [v_d\ \omega_d]^T$ are

$$\boldsymbol{F}^d_{\text{DP}} = \boldsymbol{B}^{-1}\left(\boldsymbol{M}\dot{\boldsymbol{v}}_d + \boldsymbol{A}\boldsymbol{v}_d + \boldsymbol{G} + \boldsymbol{F}_R\right)/r_s \tag{30}$$

$$\begin{aligned}\boldsymbol{T}_D &= r_s\boldsymbol{F}^d_{\text{DP}} + \hat{\boldsymbol{T}}_{De} \\ &= \boldsymbol{B}^{-1}\left(\boldsymbol{M}\dot{\boldsymbol{v}}_d + \boldsymbol{A}\boldsymbol{v}_d + \boldsymbol{G} + \boldsymbol{F}_R\right) + \hat{\boldsymbol{T}}_{De}.\end{aligned} \tag{31}$$

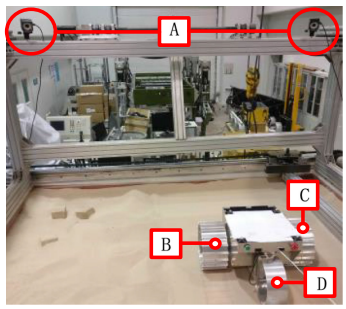

Fig. 13. WMR and motion capture system. (A) Camera. (B) Left driving wheel. (C) Right driving wheel. (D) Follower wheel.

In practical applications, a PID controller is also applied to help the WMR tracking the desired velocity and the torque inputs are

$$\begin{aligned}\boldsymbol{\tau} = \boldsymbol{T}_D + \boldsymbol{\tau}_e = \boldsymbol{T}_D + \boldsymbol{B}^{-1}\boldsymbol{M} \\ \times\left(\boldsymbol{K}_P\boldsymbol{v}_e + \boldsymbol{K}_I\int_{t_0}^{t}\boldsymbol{v}_e d\tau + \boldsymbol{K}_D\dot{\boldsymbol{v}}_e\right)\end{aligned} \tag{32}$$

where $\boldsymbol{v}_e = \boldsymbol{v}_d - \boldsymbol{v}_c$ denotes the error, $\boldsymbol{v}_c$ indicates the current velocity of the WMR, $\boldsymbol{\tau}_e$ is the torque generated by PID controller; $\boldsymbol{K}_P$, $\boldsymbol{K}_I$, and $\boldsymbol{K}_D$ are all diagonal positive-definite gain matrices of the PID controller.

The overall velocity tracking control system is illustrated in Fig. 12. After adding a kinematic controller that transforms the reference trajectory into the variable desired velocity, the system can also be expanded into a trajectory tracking control system, satisfying more demands on planetary exploration.

B. Parameter Identification of RC Models

According to (5), *RC* is required for calculating the desired driving torque. The *RC* models have been proposed in Section IV. In this part, we identified their parameters for the driving torque estimation.

A test bed with motion capture system and a WMR with two driving and a follower wheels (see Fig. 13) are used for parameter identification. The sinkage and linear/angular velocities of the WMR were measured by motion capture system (including four cameras) which can be replaced by a visual odometry module in the practical use; the wheel rotation speeds were

Manuscript 3128 submitted to 2020 IEEE/RSJ International Conference on Intelligent Robots and Systems. Received May 21, 2020.

TABLE V
EQUIVALENT SLOPE VIA APPLYING TANGENTIAL LOAD AND THE CORRESPONDING AVERAGE SLIP RATIO

Code name	Tangential component of gravity (N)	Equivalent slope (°)	Average slip ratio
Slope I	0.0	0.00	0.018
Slope II	9.8	1.91	0.119
Slope III	19.6	3.82	0.248
Slope IV	29.4	5.74	0.413
Slope V	39.2	7.66	0.601

detected by encoders; and the slip ratios of driving wheels were then calculated using these values. The forces of wheel–terrain interaction and driving moments were measured by six-axis F/T sensors.

Both driving wheels of the WMR are controlled to rotate at a constant speed (0.1 rad/s) for about 60 s. For simulating the situations on diverse slopes (see Table V), certain tangential pulls equivalent to the tangential components of gravity of the WMR on these slopes are applied to the robot body by suspending different weights through a fixed pulley. By using this method, the repeatability of experimental results can be ensured.

1) Parameter Identification of the Linearized-Form Model: The steps of identifying the slope and intercept of the linearized model (16a) are as follows:

1) calculate the *RC*(*t*) by substituting the recorded $F_N(t)$, $F_{\mathrm{DP}}(t)$ and $T_D(t)$ into (9);
2) linearly fit *RC* with *s* through least square method, deriving the slope and intercept of the model.

For the tested WMR, the two driving wheels are of the same shape, and the parameters of them should be equal. In this case, we took average of these identified parameters and eventually obtained: $RC_0^s = 0.3303$, $k_{RC}^s = 0.1950$.

2) Parameter Identification of Terramechanics Model: Based on the study in [52], the value of c_3 is assumed to be zero, and $\boldsymbol{P}_{\mathrm{I}} = \{K_s, n_0, n_1\}$, $\boldsymbol{P}_{\mathrm{II}} = \{c, \varphi, K\}$, and $\boldsymbol{P}_{\mathrm{III}} = \{c_1, c_2\}$ of terramechanics models are identified by substituting the measured data for *z*(*t*), $F_N(t)$, $F_{\mathrm{DP}}(t)$, and $T_D(t)$ into (19). The whole steps of parameter identification are as follows.

1) Derive the initial value of $\boldsymbol{P}_{\mathrm{I}}$ by setting the initial value of $\boldsymbol{P}_{\mathrm{III}} = \{0.5, 0\}$ and neglecting the effects of $\boldsymbol{P}_{\mathrm{II}}$ through using $F_N \approx rb\int_{\theta_2}^{\theta_1} \sigma(\theta)\cos\theta d\theta$.
2) Derive or update the value of $\boldsymbol{P}_{\mathrm{II}}$ through the set or newly calculated $\boldsymbol{P}_{\mathrm{I}}$ and $\boldsymbol{P}_{\mathrm{III}}$.
3) Update the value of $\boldsymbol{P}_{\mathrm{III}}$ by newly calculated $\boldsymbol{P}_{\mathrm{I}}$ and $\boldsymbol{P}_{\mathrm{II}}$.
4) Update the value of $\boldsymbol{P}_{\mathrm{I}}$ by newly calculated $\boldsymbol{P}_{\mathrm{II}}$ and $\boldsymbol{P}_{\mathrm{III}}$.
5) Iteratively derive $\boldsymbol{P}_{\mathrm{I}}$, $\boldsymbol{P}_{\mathrm{II}}$ and $\boldsymbol{P}_{\mathrm{III}}$ by repeating the steps from *ii* to *iv* until both absolute errors of c_1 and c_2 between two iterations smaller than a tiny positive value δ.

Let $\delta = 0.001$. The iteratively identified parameters of the terramechanics models are shown in Table VI.

C. Experimental Validation of the System

In this part, we experimentally verify the proposed *RC* models and compare them with the other *RC* estimation methods [52], [53] based on the recorded data. After that, the linearized model of *RC* is used for online estimating T_D due to its better efficiency and accuracy as demonstrated in the previous tests. The tracking control system shown in Fig. 12 is also tested experimentally.

TABLE VI
IDENTIFIED PARAMETERS OF TERRAMECHANICS MODEL

Terrain parameter	Value	Wheel parameter	Value
K_s (kPa/m^n)	2499	n_0	0.9649
K	1.89×10^{-4}	n_1	1.337
c (kPa)	250	c_1	0.3921
φ (°)	37.85	c_2	-0.2501
		c_3	0

TABLE VII
COMPUTATION TIME, NUMBERS OF PARAMETERS, VARIABLES, AND ERRORS OF THE *RC* MODELS

RC model	Computation time (μs)	Parameters	Variables	Error
Linearized-form (16a)	0.0128	RC_0^s, k_{RC}^s	s	2.1%
Integral-form (24)	42.3	K_s, K, φ, n_0, n_1, c_1, c_2, c_3	z, s	8.5%
Explicit-form (27)	0.129	c_1, c_2, c_3	z, s	4.6%

1) Offline RC Estimation: Let the WMR move on various slopes with both driving wheels rotating at a constant speed (0.1 rad/s). The *RC* is measured and also estimated offline using the *RC* models. The average computation time for estimating a single *RC* in MATLAB R2016b on a computer equipped with Intel(R) Core (TM) i5-7500 CPU and 8 GB RAM, the estimation errors of *RC*, the number of parameters, and the variables in the models are all listed in Table VII.

The linearized model with one variable and two parameters can be computed more efficiently than a terramechanics model with two variables and at least three parameters. The computation time for the former (0.0128 μs) is less than those of the latter by one or two orders of magnitude (42.3 μs, 0.129 μs). The computation time of 0.0128 μs is better than 0.129 μs in the sense that significantly less computation is needed with the proposed scheme. This does not mean that the 0.129 μs is insufficient for the experimental WMR traveling slowly at around 14.5 mm/s equipped with CUP of 16155 MIPS. However, for the planetary exploration rovers, as the computing resources are limited (CPUs of Rocky 7 Rover and Curiosity Rover: 103 MIPS [56] and 240 MIPS [57], respectively), the computation efficiency is quite important to realize real-time control and leave more computing resources for other tasks, such as visual odometry and online path planning.

The estimation errors by using integral-form and explicit-form models are respectively 8.5% and 4.6%. They are both larger than the one by using linearized-form model (2.1%).

Manuscript 3128 submitted to 2020 IEEE/RSJ International Conference on Intelligent Robots and Systems. Received May 21, 2020.

The larger error of *RC* is primarily caused by the error in the measurement of z. However, the inaccuracy of z measurement cannot be improved significantly by changing the sensor as the actual wheel sinkage is influenced by both unexpected change of the sand surface level and lugs entering and leaving the terrain. Generally speaking, the explicit-form model would inherently lose accuracy as compared to the integral form when experimental data are not available. However, in this article, the explicit-form model was fitted using the experimental data. As the explicit-form model is less sensitive to the measurement error of the wheel sinkage with calculating the value of $\sigma(\theta)$, it gives less errors than the integral form model. It is significant to decrease the error of *RC* estimation in order to realize high-performance velocity tracking. For the experimental WMR, the average values of F_N for both of the driving wheels are 101 N, and the wheel's shearing radius, r_s, is 0.145 m. Substituting these values into (5), we obtained that the 2.1% and 4.6% estimation errors of *RC* can result in 0.22 and 0.47 N·m errors of T_D, respectively. In turn they can lead to maximum acceleration errors of 98.7 and 216.1 mm/s^2 for the WMR with a mass of 30 kg. As the desired linear velocity of the experimental WMR is small (14.5 mm/s), the integral of the resulting acceleration error can cause obvious velocity tracking error. According to Fig. 15, the combined velocity tracking error is a bit smaller than 10% under the 2.1% estimation errors of *RC*. The sensors have been selected with adequate accuracy to meet the requirement of control and to ensure that the differences reported throughout the article are statistically significant. Based on the specifications from the sensor manuals, we calculated that the measurement errors of force, linear velocity and wheel rotation speed are less than 0.1 N, 0.1 mm/s, and 0.005 rad/s, respectively. According to (16a) and (9), the maximum errors of sensors theoretically result in 0.47% and 0.21% errors of *RC* and T_D, which are much less than their expected estimation errors. Therefore, the measurement errors are negligible, and the differences listed in Table VII are statistically significant.

During operation, *RC* is generally considered to be zero [25], [26] or a nonzero constant [54]. Therefore, we compared the variable *RC* in the linearize model (16a) with the zero *RC* and a constant value ($RC = 0.2706$). $RC_{\rm Est}$ and $RC_{\rm max}$ are defined as the estimated and maximum *RC*s. The relative error is calculated as $(|RC - RC_{\rm Est}|/RC_{\rm max}) \times 100\%$. Similarly, we define $\hat{T}_{\rm D}$ and $T_D{\rm max}$ as the estimated and maximal T_Ds. The relative error is then calculated as $|T_D - \hat{T}_{\rm D}|/T_{D\rm max} \times 100\%$. In our experiments, the values of $RC_{\rm max}$ and $T_D{\rm max}$ were approximately 0.7 and 13 N·m. The results are listed in Table VIII, where the variable *RC* model is more accurate than the zero and nonzero-constant *RC* models. The errors of the variable *RC* ($\leq$2.1%) model are smaller than the errors of the constant *RC* model (2.3%–22.6%), and the estimation errors of T_D when using variable *RC* ($\leq$1.8%) are also smaller than the errors when using zero *RC* (5.7%–27.4%) and constant *RC* (2.1%–16.9%).

By combing Tables VII and VIII, it can be clearly seen that the proposed linearized-form *RC* model is more accurate and efficient. The terramechanics models are feasible, but their accuracies and efficiencies are lower than the linearized-form model during the operation phase.

TABLE VIII
ESTIMATION ERRORS OF *RC* AND T_D BY USING THE ZERO, CONSTANT AND VARIABLE *RC*S UNDER VARIOUS SLIP RATIO

Slip ratio		0.0	0.1	0.2	0.4	0.6
Error of *RC*	Constant *RC*	18.9%	10.7%	2.3%	8.2%	22.6%
	Variable *RC*	0.2%	1.8%	1.2%	1.0%	2.1%
Error of $T_{\rm D}$	$RC = 0$	5.7%	9.6%	16.0%	21.1%	27.4%
	Constant *RC*	16.4%	10.4%	2.1%	5.6%	16.9%
	Variable *RC*	0.1%	1.6%	0.8%	0.9%	1.8%

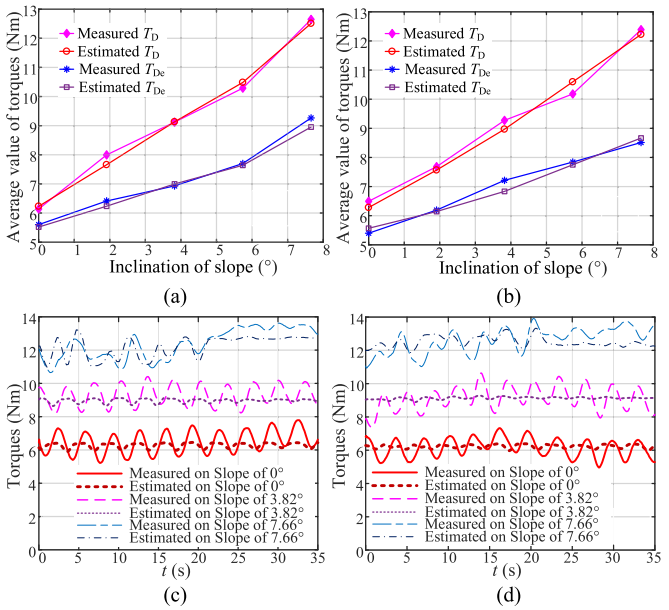

Fig. 14. T_D, T_{De} and τ of WMR on various slopes; (a) and (c) are of the left wheel, while (b) and (d) are of the right wheel.

2) Online T_D Estimation and Velocity Tracking: According to the results demonstrated in Tables VII and VIII, the linearized-form *RC* model is used for online estimation of T_D due to its high accuracy and efficiency. The WMR moves straight on various slopes (see Table IV), and the desired velocities are: v_d = 14.5 mm/s, $\omega_d = 0$. The results of real-time *RC* estimation can be seen in Fig. 14.

For both driving wheels, although T_{De} and T_D of each wheel increase significantly about 0.45 and 0.77 N·m with a slight increase of slope of 1°, the average estimation errors are still less than 6% and 4%, as shown in Fig. 14(a) and (b). Moreover, Fig. 14(c) and (d) demonstrate that each estimated T_D plays a dominant role in the torque input τ (larger than 89%), and the PID controller slightly adjust the value of torque input for tracking the desired velocity.

The tracking results can be seen in Fig. 15. Wheel lugs that alternately enter in and leave from the terrain generate approximately sinusoidal fluctuations of T_D, $F_{\rm DP}$, and F_N, resulting in fluctuations of velocity and slip ratio [34], [35]. However, the WMR still tracked the desired velocities accurately on various

Manuscript 3128 submitted to 2020 IEEE/RSJ International Conference on Intelligent Robots and Systems. Received May 21, 2020.

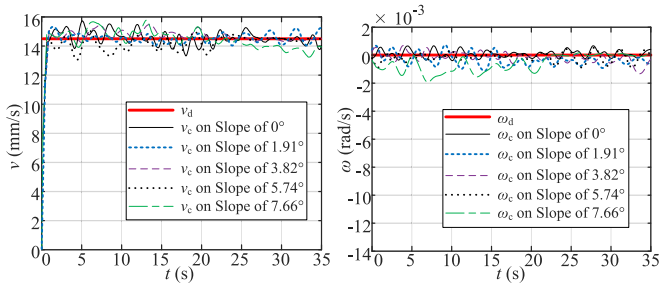

Fig. 15. Linear and angular velocities of the WMR applied the control system in Fig. 12 on various slopes shown in Table IV.

sandy slopes (the values of linear velocity error are less than 1.39 mm/s (10%) in the steady state, and the values of angular velocity error are less than 1.9×10^{-3} rad/s).

As demonstrated by the experimental results, the linearized-form *RC* model is more suitable for real-time control for WMRs, as T_D can be estimated more efficiently and accurately with it. A simple yet accurate dynamic tracking control system for a WMR on deformable terrain is successfully implemented by applying this estimation method.

VI. Velocity Compensation With Slip Ratio Estimation

The linearized-form *RC* model is not only used for estimating the desired driving torque, but also used to estimate the slip ratio and compensate for the velocity loss due to slip for motion control of WMRs, in situations where visual odometry does not work properly.

A. Slip Ratio Estimation by Using RC

The new method of estimating slip ratio of each driving wheel using *RC* linearized model is proposed in this section.

Assume that in this section, the actual velocity of the WMR cannot be directly measured and accordingly, the wheel slip ratios are difficult to detect. In this situation which occurs in practice, the slip ratio of a wheel can be estimated in real time using the *RC* model (16a) as follows:

$$s = \frac{1}{k_{RC}^{s}} \left(RC - RC_0^{s} \right). \tag{33}$$

For a planetary rover that moves slowly with low angular wheel accelerations during a mission, the *RC* can be estimated by current moment τ_c, wheel–terrain interaction forces F_{DP} and F_N as follows:

$$RC_{\mathrm{Est}} = \tau_c / \left(F_N r_s \right) - F_{\mathrm{DP}} / F_N. \tag{34}$$

After combing (34) and (35), the slip ratio of a wheel is

$$\hat{s} = \frac{1}{k_{RC}^{s}} \left(\frac{\tau_c}{F_N r_s} - \frac{F_{\mathrm{DP}}}{F_N} - RC_0^{s} \right). \tag{35}$$

B. Velocity Compensation Control

In order to eliminate the slow-down effect of wheel slip, we studied the velocity compensation method based on the estimated slip ratio, and then applied it to tracking control of the WMR.

For a WMR of $(2, 0)$ type moving on a soft slope, the kinematic model of it can be written as follows:

$$\boldsymbol{v} = \boldsymbol{J}\dot{\boldsymbol{\vartheta}} - \boldsymbol{J}\boldsymbol{s}\dot{\boldsymbol{\vartheta}} \tag{36}$$

where $\boldsymbol{\vartheta} = [\,\vartheta_1 \;\vartheta_2\,]^T$ indicates the rotation angles of the two driving wheels, $\boldsymbol{s}$ which is a diagonal matrix denotes the slip ratios of the two wheels and $\boldsymbol{J}$ is the Jacobian matrix. The actual expressions of $\boldsymbol{s}$ and $\boldsymbol{J}$ are respectively

$$\boldsymbol{s} = \begin{bmatrix} s_1 & 0 \\ 0 & s_2 \end{bmatrix} \boldsymbol{J} = \frac{r_s}{2} \begin{bmatrix} 1 & 1 \\ -1/d_1 & 1/d_1 \end{bmatrix}$$

Based on (35), $\boldsymbol{s}$ is estimated in real time as

$$\hat{\boldsymbol{s}} = \frac{1}{k_{RC}^{s}} \begin{bmatrix} \frac{\tau_c^1}{F_N^1 r_s} - \frac{F_{\mathrm{DP}}^1}{F_N^1} - RC_0^{s} & 0 \\ 0 & \frac{\tau_c^2}{F_N^2 r_s} - \frac{F_{\mathrm{DP}}^2}{F_N^2} - RC_0^{s} \end{bmatrix}. \tag{37}$$

By combining (36) and (37), the current velocity of the WMR can be estimated through the current rotational speeds of the wheels $\dot{\boldsymbol{\vartheta}}_c = [\,\dot{\vartheta}_c^1 \;\dot{\vartheta}_c^2\,]^T$ as follows:

$$\hat{\boldsymbol{v}}_c = \boldsymbol{J}\dot{\boldsymbol{\vartheta}}_c - \boldsymbol{J}\hat{\boldsymbol{s}}\dot{\boldsymbol{\vartheta}}_c. \tag{38}$$

After substituting (38) into (32), the control law of velocity tracking becomes

$$\begin{aligned} \boldsymbol{\tau} &= \boldsymbol{B}^{-1} \left(\boldsymbol{M}\dot{\boldsymbol{v}}_d + \boldsymbol{A}\boldsymbol{v}_d + \boldsymbol{G} + \boldsymbol{F}_R \right) + \bar{\boldsymbol{T}}_{De}(\theta) + \boldsymbol{\tau}_e \\ &= \bar{\boldsymbol{T}}_D + \boldsymbol{\tau}_e^{\vartheta} + \boldsymbol{\tau}_s \end{aligned} \tag{39}$$

where $\bar{\boldsymbol{T}}_{De}(\theta)$ indicates the extra driving torques which cannot be calculated by (29) anymore due to the inability of slip ratio measurement, but is looked up from a table related to the pitch angle θ of the WMR based on the former experimental results in Fig. 14(a) and (b). And $\boldsymbol{\tau}_e^{\vartheta} = \boldsymbol{B}^{-1}\boldsymbol{M}\boldsymbol{J}(\boldsymbol{K}_P\dot{\boldsymbol{\vartheta}}_e + \boldsymbol{K}_I\boldsymbol{\vartheta}_e + \boldsymbol{K}_D\ddot{\boldsymbol{\vartheta}}_e)$ are the PID regulated torques of angular speed, $\boldsymbol{\vartheta}_e = \boldsymbol{\vartheta}_d - \boldsymbol{\vartheta}_c$ denotes the errors, while $\boldsymbol{\tau}_s = \boldsymbol{B}^{-1}\boldsymbol{M}\boldsymbol{J}(\boldsymbol{K}_P\hat{\boldsymbol{s}}\dot{\boldsymbol{\vartheta}}_c + \boldsymbol{K}_I\hat{\boldsymbol{s}}\boldsymbol{\vartheta}_c + \boldsymbol{K}_D\hat{\boldsymbol{s}}\ddot{\boldsymbol{\vartheta}}_c)$ are the slip compensation torque, compensating the loss of velocities resulted from slip.

The overall velocity tracking control system of the WMR with slip estimation and compensation can be seen in Fig. 16.

C. Experimental Validation of Velocity Compensation

In this part, the proposed system shown in Fig. 16 is experimentally investigated.

1) Real-Time Slip Estimation: The WMR moves at a constant speed ($v = 14.5$ mm/s and $\omega = 0$) on various slopes shown in Table V. The slip ratios of two driving wheels are estimated by substituting the detected wheel–terrain interaction forces and torques into (35), and measured by combining motion capture system and encoders. The experimental results are shown in Table IX and Fig. 17.

According to Table IX, all the average estimation errors of slip ratio on various slopes are very small (smaller than 6%). As to the dynamic process shown in Fig. 17, although the estimation errors are very large at the beginning when the wheels just start

Manuscript 3128 submitted to 2020 IEEE/RSJ International Conference on Intelligent Robots and Systems. Received May 21, 2020.

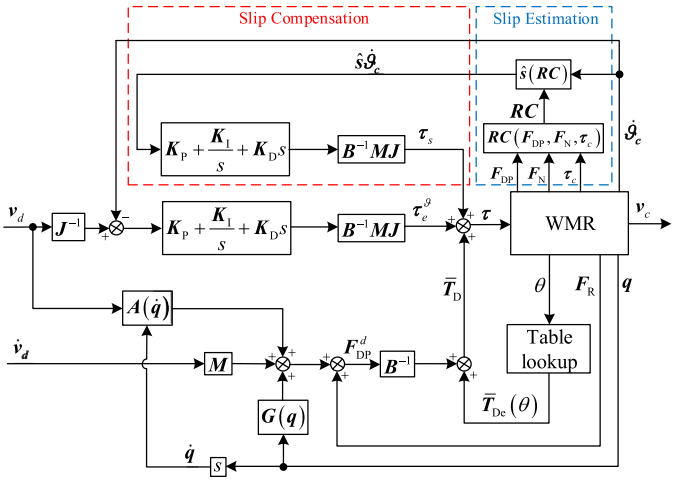

Fig. 16. Velocity tracking control system for the WMR with slip estimation and velocity compensation by using *RC* model ($\boldsymbol{F}_{\mathrm{DP}}$, $\boldsymbol{F}_N$, $\boldsymbol{\tau}_c$, $\dot{\boldsymbol{\vartheta}}_c$, $\boldsymbol{F}_R$, and θ are measured quantities).

TABLE IX
AVERAGE ESTIMATION ERRORS OF SLIP RATIO OF THE TWO DRIVING WHEELS ON VARIOUS SLOPES

Slope	0°	1.91°	3.82°	5.74°	7.66°
Left wheel	1.5%	4.7%	4.3%	5.0%	5.3%
Right wheel	1.6%	4.5%	4.3%	5.1%	5.9%

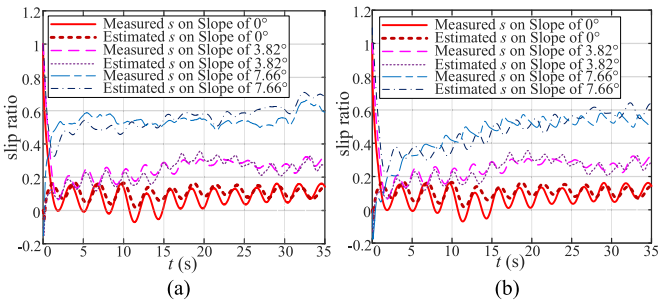

Fig. 17. Measured and estimated slip ratio on various slopes shown in Table IV, (a) is of left wheel, (b) is of right wheel.

rotating, the estimated and measured slip ratios are almost of the same value in the steady state (the error is less than 9%). Moreover, both the estimated and measured slip ratios oscillate at the same frequency in the steady state.

Considering that the slip ratio is also defined as the difference between the commanded longitudinal motion and actual longitudinal motion at the WMR level, the measured travel distanceD_m and the estimated travel distance D_e [40], [44] are substituted into (40) to approximate typical values of the slip estimation error (see Table X)

$$e_{\mathrm{slip}} = \frac{|D_m - D_e|}{D_m} \times 100\%. \tag{40}$$

According to Tables IX and X, the proposed slip estimation method is more accurate, as its errors (<6%) are generally

TABLE X
TYPICAL ERROR VALUES FOR SLIP ESTIMATION REPORTED IN LITERATURE

Methods	Enhanced odometry[44]	NAVCAM-based odometry [40]	Slippage correction odometry [44]
Errors	13%	9%	6%

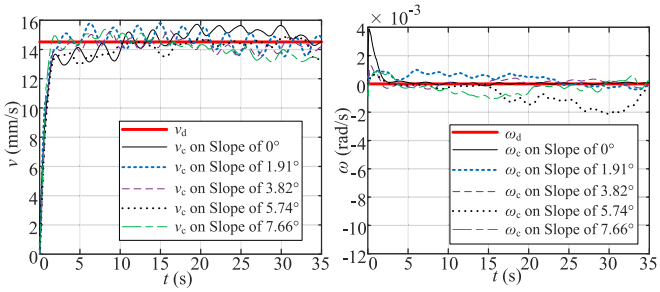

Fig. 18. Linear and angular velocities of the WMR applied control system with velocity compensation (see Fig. 16) on various slopes.

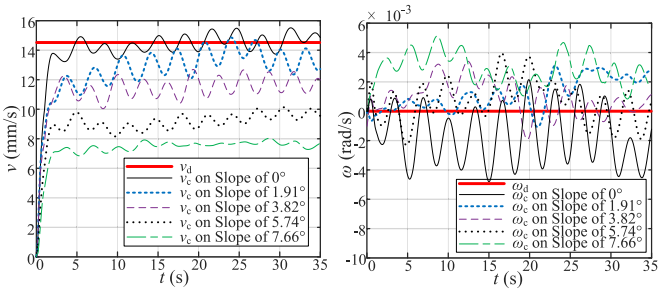

Fig. 19. Linear and angular velocities of the WMR applied control system without velocity compensation on various slopes.

smaller than the typical errors reported in the literature (6–13%) [40], [44].

2) Real-Time Velocity Compensation: Similarly, the WMR moves on different slopes as shown in Table IV. The desired linear and angular velocities of the WMR are respectively 14.5 mm/s and 0.

The experimental results shown in Fig. 18 demonstrate that the proposed velocity compensation control algorithm is feasible. On variable slopes, the values of linear velocity tracking error are all smaller than 1.45 mm/s (10%) in the steady state, and the values of angular velocity tracking error are all smaller than 2.0×10^{-3} rad/s.

For comparison, the control method without velocity compensation is also tested. The feedback of the PID controller is wheel rotation speed, and the wheel slip is not considered in this semi-closed-loop control system. The results are shown in Fig. 19. By comparing Figs. 18 with 19, it can be clearly seen that on variable slopes, the values of velocity tracking error significantly reduce after applying velocity compensation. The value of linear velocity tracking error reduces from generally more than 20% to less than 10%, and the reduction becomes more significant as the slope increases. On the steepest slope (Slope V, 7.66°), the value of linear velocity tracking error

Manuscript 3128 submitted to 2020 IEEE/RSJ International Conference on Intelligent Robots and Systems. Received May 21, 2020.

reduces from 48% to 10%. The value of angular velocity tracking error also conspicuously falls. On the smallest slope (Slope I, 0.00°) and the steepest one (Slope V, 7.66°), the maximum values of the errors decrease more than 97% and 78%, respectively. Therefore, the feedforward based on the estimated slip ratio is required for compensating the velocity loss due to slip.

The above experimental results illustrate that the proposed slip estimation method by using *RC* is feasible on sandy terrain and can be applied to tracking control of WMRs for compensating the velocity loss due to slip.

VII. Conclusion

This article defined a variable (as opposed to constant) formulation of *RC*. This formulation is accompanied with the relevant models, estimations of driving torque and slip ratio, and the application of these models to velocity control of a WMR.

The current trends in the literature were geared toward more physics-based models that were suitable for online use, but these models contain too many parameters that need to be identified using a large number of measurements, in particular the most challenging wheel sinkage. The linearized-form *RC* model had the characteristics of simplicity yet high efficiency and accuracy, as it is an intrinsic model, however, the generalization of this model should be investigated. We partially validated that it is suitable for wheels with different dimensions.

The presented tracking control approach that relies on linearized-form *RC* model requires the measurements of slip ratios, forces, and torques. This model does not need the wheel sinkage that is the most difficult to measure, improving the practicality. Although accurate measurements of the other variables are still challenging in practice, some WMRs for planetary exploration realized such measurements, including the experimental microrover in [20], El-Dorado II [52] and the Lunar Rover Prototype in [58]; the slip ratios were calculated based on the wheel linear velocities measured by visual odometry and wheel rotation speeds measured by encoders, whereas the forces and torques were measured by F/T sensors.

Our analysis and experimental data lead to the following conclusions.

1) The traction coefficient *TC* is less sensitive to wheel parameters; thus, *RC* has a dominant role in determining the pull coefficient of a wheel *PC* (*PC* = *TC*–*RC*).
2) When considering *RC* as a linear function of the slip ratio, extra driving torque T_{De}, desired driving torque T_D, and slip ratio *s* can be estimated with adequate accuracy and low calculation cost.
3) Compared with T_D estimation methods using traditional terramechanics-based methods [30], [53], the proposed method using the defined variable *RC* is more accurate and effective, especially on sandy terrain, and has been applied to dynamic tracking control system of WMRs.
4) Compared with generally used slip estimation methods [40], [44], the proposed slip estimation method is also more accurate and effective, especially on sandy terrain, and allows the application of velocity compensation to velocity control, which significantly improves the accuracy of the system if the velocity of WMR cannot be measured.

The proposed methods are limited by several factors, which are as follows.

1) The parameters of the linearized *RC* model are influenced by wheel parameters, terrain parameters, motion-state variables, and other factors. At present, the model has only been validated on soft dry sand.
2) The determination of these parameters will require high-fidelity terramechanics models, or experimental data about forces and driving torque under various slip ratios.
3) The effectiveness of the proposed method for wheels that slip so severely that they sink at a high entrance angle remains to be verified.
4) F/T sensors are utilized for implementing the proposed estimation method in this work. These are feasible to use in Earth-bound vehicles but the application to planetary exploration rovers requires the protection of the sensors from extreme environments (high and low temperatures, cosmic radiation, etc.).

Future work may address the generalization of the proposed *RC* models for different WMRs on different terrains, as well as the novel approaches of measuring slip ratios, forces, and torques online in real-time.

References

[1] D. F. Blake *et al.*, "Curiosity at gale crater, mars: Characterization and analysis of the rocknest sand shadow," *Science*, vol. 341, no. 6153, Sep. 2013, Art. no. 1239505.
[2] M. Maimone, Y. Cheng, and L. Matthies, "Two years of visual odometry on the mars exploration rovers," *J. Field Robot.*, vol. 24, no. 3, pp. 169–186, Mar. 2007.
[3] D. Wettergreen, D. Jonak, D. Kohanbash, S. Moreland, S. Spiker, and J. Teza, "Field experiments in mobility and navigation with a lunar rover prototype," in *Field and Service Robotics*. New York, NY, USA: Springer, Mar. 2010, pp. 489–498.
[4] D. Helmick, A. Angelova, and L. Matthies, "Terrain adaptive navigation for planetary rovers," *J. Field Robot.*, vol. 26, no. 4, pp. 391–410, Feb. 2009.
[5] M. Heverly *et al.*, "Traverse performance characterization for the Mars Science Laboratory rover," *J. Field Robot.*, vol. 30, no. 6, pp. 835–846, Sep. 2013.
[6] D. M. Helmick, Y. Cheng, D. S. Clouse, and L. H. Matthies, "Path following using visual odometry for a Mars rover in high-slip environments," in *Proc. IEEE Aerosp. Conf*, vol. 2, Mar. 2004, pp. 772–789.
[7] L. Caracciolo, A. de Luca, and S. Iannitti, "Trajectory tracking control of a four-wheel differentially driven mobile robot," in *Proc. IEEE Int. Conf. Robot. Autom.*, May. 1999, pp. 2632–2638.
[8] R. González, F. Rodríguez, and J. L. Guzmán, *Autonomous Tracked Robots in Planar Off-Road Conditions—Modelling, Localization, and Motion Control* (Studies in Systems, Decision and Control), vol. 6. New York, NY, USA: Springer, 2014.
[9] F. Zhou *et al.*, "Simulations of Mars rover traverses," *J. Field Robot.*, vol. 31, no. 1, pp. 141–160, Sep. 2014.
[10] L. Ding, H. Gao, Z. Deng, and W. Li, "Advances in simulation of planetary wheeled mobile robots," in *Mobile Robots–Current Trends*, Z. Gacovski, Ed. Vienna, Austria: InTech Press, 2011, pp. 375–402.
[11] R. Krenn, A. Gibbesch, and G. Hirzinger, "Contact dynamics simulation of rover locomotion," in *Proc. 9th Int. Symp. Artif. Intell., Robot. Autom. Space*, Feb. 2008.
[12] B. Schäfer, A. Gibbesch, R. Krenn, and B. Rebele, "Planetary rover mobility simulation on soft and uneven terrain," *J. Veh. Syst. Dyn.*, vol. 48, no. 1, pp. 149–169, Dec. 2010.

Manuscript 3128 submitted to 2020 IEEE/RSJ International Conference on Intelligent Robots and Systems. Received May 21, 2020.

[13] D. S. Apostolopoulos, "Analytical configuration of wheeled robotics locomotion," Carnegie Mellon University, Pittsburgh, PA, USA, Tech. Rep. CMU-RI-TR-01-08, Apr. 2001.

[14] M. Sutoh, K. Nagaoka, K. Nagatani, and K. Yoshida, "Design of wheels with grousers for planetary rovers traveling over loose soil," *J. Terramechanics*, vol. 50, nos. 5/6, pp. 345–353, Jul. 2013.

[15] A. C. Leite and B. Schäfer, "On multi-objective optimization of planetary exploration rovers applied to ExoMars-type rovers," in *Proc. 11th Symp. Adv. Space Technol. Robot. Automat., ESA/ESTEC*, Apr. 2011.

[16] Z. Liang, J. Chen, and Y. Wang, "Equivalent acceleration imitation for single wheel of manned lunar rover by varying torque on earth," *IEEE/ASME Trans. Mechatronics*, vol. 25, no. 1, pp. 282–293, Feb. 2020.

[17] R. Gonzalez and K. Iagnemma, "Slippage estimation and compensation for planetary exploration rovers. State of the art and future challenges," *J. Field Robot.*, vol. 35, pp. 564–574, Oct. 2017.

[18] G. Ishigami, A. Miwa, K. Nagatani, and K. Yoshida, "Terramechanics-based model for steering maneuver of planetary exploration rovers on loose soil," *J. Field Robot.*, vol. 24, no. 3, pp. 233–250, Mar. 2007.

[19] L. Ding, H. Gao, Z. Deng, and J. Tao, "Wheel slip-sinkage and its estimation model of lunar rover," *J. Central South Univ. Technol.*, vol. 17, no. 1, pp. 129–135, Feb. 2011.

[20] K. Iagnemma and S. Dubowsky, "Traction control of wheeled robotic vehicles in rough terrain with application to planetary rovers," *Int. J. Robot. Res.*, vol. 23, nos. 10/11, pp. 1029–1040, Oct. 2004.

[21] D. Lhomme-Desages, C. Grand, J.-C. Guinot, and F. B. Amar, "Doppler-based ground speed sensor fusion and slip control for a wheeled rover," *IEEE/ASME Trans. Mechatronics*, vol. 14, no. 4, pp. 484–492, Mar. 2009.

[22] L. Ojeda, J. Borenstein, G. Witus, and R. Karlsen, "Terrain characterization and classification with a mobile robot," *J. Field Robot.*, vol. 23, no. 2, pp. 103–122, Mar. 2006.

[23] A. Gallina, R. Krenn, M. Scharringhausen, T. Uhl, and B. Schäfer, "Parameter identification of a planetary rover wheel–soil contact model via a Bayesian approach," *J. Field Robot.*, vol. 31, no. 1, pp. 161–175, Sep. 2014.

[24] L. Ding, Z. Deng, H. Gao, J. Tao, K. Iagnemma, and G. Liu, "Interaction mechanics model for rigid driving wheels of planetary rovers moving on sandy terrain with consideration of multiple effects," *J. Field Robot.*, vol. 32, no. 6, pp. 827–859, 2015.

[25] G. D. White, R. M. Bhatt, P. T. Chin, and V. N. Krovi, "Experimental evaluation of dynamic redundancy resolution in a nonholonomic wheeled mobile manipulator," *IEEE/ASME Trans. Mechatronics*, vol. 14, no. 3, pp. 349–357, Jun. 2009.

[26] Z. Li, S. S. Ge, and A. Ming, "Adaptive robust motion/force control of holonomic-constrained nonholonomic mobile manipulators," *IEEE Trans. Syst., Man, Cybern. B, Cybern.*, vol. 37, no. 3, pp. 607–616, May 2007.

[27] L. Ding, H. Gao, Z. Deng, K. Nagatani, and K. Yoshida, "Experimental study and analysis on driving wheels' performance for planetary exploration rovers moving in deformable soil," *J. Terramechanics*, vol. 48, no. 1, pp. 27–45, Feb. 2011.

[28] D. Lhomme-Desages, C. Grand, and J-C. Guinot, "Trajectory control of a four-wheel skid-steering vehicle over soft terrain using a physical interaction model," in *Proc. IEEE Int. Conf. Robot. Automat.*, Apr. 2007, pp. 1164–1169.

[29] M. G. Bekker, *Introduction to Terrain–Vehicle Systems*. Ann Arbor, MI, USA: Univ. Michigan Press, Oct. 1969.

[30] J. Y. Wong and A. R. Reece, "Estimation of rigid wheel performance based on the analysis of soil-wheel stresses: Part I-performance of driven rigid wheels," *J. Terramechanics*. vol. 4, no. 1, pp. 81–98, 1967.

[31] K. Iagnemma, S. Kang, H. Shibly, and S. Dubowsky, "Online terrain parameter estimation for wheeled mobile robots with application to planetary rovers," *IEEE Trans. Robot.*, vol. 20, no. 5, pp. 921–927, Oct. 2004.

[32] L. Ray, "Estimation of terrain forces and parameters for rigid-wheeled vehicles," *IEEE Trans. Robot.*, vol. 25, no. 3, pp. 717–726, Jun. 2009.

[33] L. Ding, K. Yoshida, K. Nagatani, H. Gao, and Z. Deng, "Parameter identification for planetary soil based on a decoupled analytical wheel-soil interaction terramechanics model," in *Proc. IEEE/RSJ Int. Conf. Intelligent Robots Syst.*, Oct. 2009, pp. 4122–4127.

[34] R. A. Irani, R. J. Bauer, and A. Warkentin, "Dynamic wheel-soil model for lightweight mobile robots with smooth wheels," *J. Intell. Robot. Syst.*, vol. 71, no. 2, pp. 179–193, Sep. 2013.

[35] R. A. Irani, R. J. Bauer, and A. Warkentin, "A dynamic terramechanic model for small lightweight vehicles with rigid wheels and grousers operating in sandy soil," *J. Terramechanics*, vol. 48, no. 4, pp. 307–318, Aug. 2011.

[36] N. Seegmiller and A. Kelly, "High-fidelity yet fast dynamic models of wheeled mobile robots," *IEEE Trans. Robot.*, vol. 32, no. 3, pp. 614–625, Jun. 2016.

[37] L. Ojeda, G. Reina, and J. Borenstein, "Experimental results from FLEXnav: An expert rule-based dead-reckoning system for Mars rovers," in *Proc. IEEE Aerosp. Conf.*, 2004, vol. 2, pp. 816–825.

[38] D. M. Helmick, S. I. Roumeliotis, Y. Cheng, D. S. Clouse, M. Bajracharya, and L. H. Matthies, "Slip-compensated path following for planetary exploration rovers," *Adv. Robot.*, vol. 20, no. 11, pp. 1257–1280, Apr. 2006.

[39] B. L. Chang and D. Wang, "GPS-based path following control for a car-like wheeled mobile robot with skidding and slipping," *IEEE/ASME Trans. Mechatronics*, vol. 13, no. 4, pp. 480–484, Mar. 2008.

[40] S. Lowry *et al.*, "Visual place recognition: A survey," *IEEE Trans. Robot.*, vol. 32, no. 1, pp. 1–19, Feb. 2016.

[41] R. Gonzalez, F. Rodriguez, J. L. Guzman, and C. Pradalier, "Combined visual odometry and visual compass for off-road mobile robots localization," *Robotica*, vol. 20, no. 6, pp. 865–878, Oct. 2012.

[42] J. Stephan, J. Fink, V. Kumar, and A. Ribeiro, "Concurrent control of mobility and communication in multirobot systems," *IEEE Trans. Robot.*, vol. 33, no. 5, pp. 1248–1254, Oct. 2017.

[43] S. Safavi, and U. A. Khan, "An opportunistic linear–convex algorithm for localization in mobile robot networks," *IEEE Trans. Robot.*, vol. 33, no. 4, pp. 875–888, Aug. 2017.

[44] G. Reina, G. Ishigami, K. Nagatani, and K. Yoshida, "Odometry correction using visual slip angle estimation for planetary exploration rovers," *Adv. Robot.*, vol. 24, no. 3, pp. 359–385, Jan. 2010.

[45] G. Ishigami, K. Nagatani, and K. Yoshida, "Path following control with slip compensation on loose soil for exploration rover," in *Proc. IEEE/RSJ Int. Conf. Intell. Robots Syst.*, Oct. 2006, pp. 5552–5557.

[46] W. Dong, W. Huo, S. K. Tso, and W. L. Xu, "Tracking control of uncertain dynamic nonholonomic system and its application to wheeled mobile robots," *IEEE Trans. Robot. Automat.*, vol. 16, no. 6, pp. 870–874, Dec. 2000.

[47] W. Dong and K. D. Kuhnert, "Robust adaptive control of nonholonomic mobile robot with parameter and nonparameter uncertainties," *IEEE Trans. Robot.*, vol. 21, no. 2, pp. 261–266, Apr. 2005.

[48] M. Chen, "Disturbance attenuation tracking control for wheeled mobile robots with skidding and slipping," *IEEE Trans. Ind. Electron.*, vol. 64, no. 4, pp. 3359–3368, Apr. 2017.

[49] L. Ding, S. Li, Y. J. Liu, C. Chen, and Z. Deng, "Adaptive neural network-based tracking control for full-state constrained wheeled mobile robotic system," *IEEE Trans. Syst. Man Cyber. Syst.*, vol. 47, no. 8, pp. 2410–2419, Aug. 2017.

[50] M. Van, "An enhanced robust fault tolerant control based on an adaptive fuzzy PID-nonsingular fast terminal sliding mode control for uncertain nonlinear systems," *IEEE/ASME Trans. Mechatronics*, vol. 23, no. 3, pp. 1362–1371, Jun. 2018.

[51] L. Ding, Z. Deng, H. Gao, J. Guo, D. Zhang, and K. D. Iagnemma, "Experimental study and analysis of the wheels' steering mechanics for planetary exploration wheeled mobile robots moving on deformable terrain," *Int. J. Robot. Res.*, vol. 32, no. 6, pp. 712–743, May 2013.

[52] L. Ding, H. Gao, Z. Liu, Z. Deng, and G. Liu, "Identifying mechanical property parameters of planetary soil using in-situ data obtained from exploration rovers," *Planet. Space Sci.*, vol. 119, pp. 121–136, Dec. 2015.

[53] H. Shibly, K. Iagnemma, and S. Dubowsky, "An equivalent soil mechanics formulation for rigid wheels in deformable terrain, with application to planetary exploration rovers," *J. Terramechanics*, vol. 42, no. 1, pp. 1–13, Jan. 2005.

[54] H. S. Bae and J. C. Gerdes, "Parameter estimation and command modification for longitudinal control of heavy vehicles," UC Berkeley, California Partners\Adv. Transportation Technol., Berkeley, CA, USA. Rep. no. TO-4202, Apr. 2003. [Online] Available: https://escholarship.org/uc/item/6s35h1ch

[55] Y. Gao, C. Spiteri, C. Li, and Y. Zheng, "Lunar soil strength estimation based on Chang'E-3 images," *Adv. Space Res.*, vol. 58, no. 9, pp. 1893–1899, Nov. 2016.

[56] A. L. Crouch, "Testability features of the MC68060 microprocessor" in *Proc. IEEE Int. Test Conf.*, Washington, DC, USA, Oct. 1994, pp. 60–69.

[57] R. W. Berger *et al.*, "The RAD750 (TM) - A radiation hardened PowerPC (TM) processor for high performance spaceborne applications," in *Proc. IEEE Aerosp. Conf.*, vol. 5, Mar. 2001, pp. 2263–2272.

[58] K. Yoshida, T. Watanabe, N. Mizuno, and G. Ishigami, "Slip, traction control, and navigation of a lunar rover," in *Proc. 7th Int. Symp. Artif. Intell., Robot. Automat. Space*, May 2003, pp. 19–23.

Manuscript 3128 submitted to 2020 IEEE/RSJ International Conference on Intelligent Robots and Systems. Received May 21, 2020.

Liang Ding (Senior Member, IEEE) was born in 1980. He received the Ph.D. degree in mechanical engineering from the Harbin Institute of Technology, Harbin, China, in 2009.

He is currently a Professor with the State Key Laboratory of Robotics and System, Harbin Institute of Technology. His current research interests include mechanics (in particular terramechanics), intelligent control, design and simulation of robotic systems, in particular for planetary exploration rovers and multi-legged robots.

Dr. Ding is currently the Associate Editor of the IEEE Access. He has served on the ISTVS Board of Directors since 2019, and was a recipient of the 2018 Outstanding Youth Program of National Natural Science Foundation of China, 2017 ISTVS Söhne-Hata-Jurecka Award, and the 2011 National Award for Technological Invention of China.

Lan Huang received the B.S. degree in mechanical engineering and automation from Northeast University, Shenyang, China, in 2016, and the M.S. degree in manufacturing engineering of aerospace vehicle in 2018 from the Harbin Institute of Technology, Harbin, China, where he is currently working toward the Ph.D. degree in aeronautical and astronautical science and technology.

His current research interests include terramechanics, dynamic modeling, and adaptive control of wheeled mobile robots.

Shu Li received the B.S. degree in information and computing science and the M.S. degree in applied mathematics from the Liaoning University of Technology, Jinzhou, China, in 2013 and 2016, respectively. He is currently working toward the Ph.D. degree in aeronautical and astronautical science and technology with the Harbin Institute of Technology, Harbin, China.

His current research interests include adaptive control, neural network control, reinforcement learning, and intelligent control of wheeled mobile robots.

Haibo Gao was born in 1970. He received the Ph.D. degree in mechanical design and theory from the Harbin Institute of Technology, Harbin, China, in 2004.

He is currently a Professor with the State Key Laboratory of Robotics and System, Harbin Institute of Technology. His current research interests include specialized and aerospace robotics and mechanisms.

Huichao Deng, photograph and biography not available at the time of publication.

Yuankai Li (Senior Member, IEEE) received the Ph.D. degree in control science and engineering from Shanghai Jiao Tong University, Shanghai, China, in 2011.

He was a Postdoctoral Fellow with the Department of Aerospace Engineering, Ryerson University, Toronto, ON, Canada, and currently is an Associate Professor with the University of Electronic Science and Technology of China, Chengdu, China. His research interests include intelligent control and signal processing for aerospace unmanned systems.

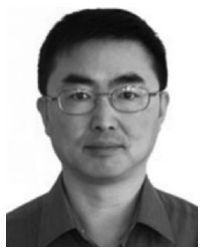

Guangjun Liu (Senior Member, IEEE) received the Ph.D. degree from the University of Toronto, Toronto, ON, Canada, in 1996.

He is currently a Professor and a Former Canada Research Chair in control systems and robotics with the Department of Aerospace Engineering, Ryerson University, Toronto. His current research interests include control systems and robotics, particularly in modular and reconfigurable robots, mobile manipulators, and aircraft systems.

Manuscript 3128 submitted to 2020 IEEE/RSJ International Conference on Intelligent Robots and Systems. Received May 21, 2020.